Kärki, Tytti; Pääkkönen, Into; Kyriakopoulos, Nikos; Timonen, Jaakko V.I.

Quasi-two-dimensional pseudo-sessile drops

Published in:
Communications Physics

DOI:
10.1038/s42005-024-01831-2

Published: 01/12/2024

Document Version
Publisher's PDF, also known as Version of record

communications physics

Article

https://doi.org/10.1038/s42005-024-01831-2

Quasi-two-dimensional pseudo-sessile drops

Check for updates

Tytti Kärki, Into Pääkkönen, Nikos Kyriakopoulos & Jaakko V. I. Timonen

Sessile drops are ubiquitous and important in technological applications. While dynamics of liquid drops have been studied under confinement, the possibility of creating sessile drops with reduced dimensionality has not been explored. Here, we demonstrate a quasi-two-dimensional (Q2D) analogy for axisymmetric sessile three-dimensional (3D) drops. The Q2D drops are created by confining liquids between parallel vertical walls, forming low aspect ratio capillary bridges deformed by gravity. Stationary Q2D drops adopt projected shapes analogous to 3D sessile drops, ranging from circular drops to puddles. When moving, the Q2D drops exhibit capillary and fluid mechanical behaviours conceptually analogous to 3D drops, including impacts and sliding. The Q2D drops also exhibit more complex phenomena such as levitation, various instabilities and pattern formation when subjected to external electric, magnetic and flow fields. The 3D-Q2D analogy suggests that the diverse and often complicated phenomena observed in 3D drops can be studied in the simplified Q2D geometry. Additionally, the Q2D confinement analogy allows exploring phenomena arising from the reduced dimensionality and the altered boundary conditions.

Sessile liquid drops are ubiquitous and diverse around us. Depending on the drop volume, properties of the liquid, and the nature of interaction with the supporting surface, drops can adopt shapes ranging from ideal spheres and puddles to highly irregular forms. It is well established how surface tension, contact angle (CA) and external forces such as gravity determine the overall equilibrium drop shape[1]. The situation is especially useful when the CA is large, leading to drops beading up and often moving nearly effortlessly on the surface[2,3]. Such non-wetting is useful in numerous applications requiring dryness and self-clean ability[4–6]. In practice, large CAs and non-wetting states can be achieved by taking advantage of the Cassie-Baxter state on superhydrophobic surfaces[5,7,8], the Leidenfrost effect[9–11], or utilizing so called fizzy drops that were discovered recently[12,13].

On the other hand, the behavior of liquid drops has been investigated also in confined geometries[14]. One particularly important geometry consists of two flat parallel plates, known as the Hele-Shaw cell[15]. Therein, depending on the wettability of the confining plates, pancake-shaped drops with large CA and concave capillary bridges with small CA can be formed and studied. The investigated phenomena include drop motion upon tilting the cell[16], falling dynamics of drops in vertical cells[14], drop coalescence[17], drop attachment to defects[18,19], and freezing dynamics of drops[20–22]. In addition, modified Hele-Shaw cell geometries with wedged cells and asymmetrical cells consisting of a combination of a flat and a cylindrical wall have been used to move, trap and elongate confined drops[16,23]. Applications for flattened confined droplets in Hele-Shaw cells can be found in microfluidic devices, where precisely sized drops can be generated, transported and used as micro-reactors to perform chemical reactions useful for example in biomedical applications[24,25]. Beyond drops and capillary bridges, motion of solid disk-shaped objects[26], liquid rivulets[27] and bubbles[14] has been studied in the Hele-Shaw cells, demonstrating the versatility of phenomena possible to study in confined geometries. Although many drop phenomena have been studied in reduced dimensionality, for example the concept of sessile drops with reduced dimensionality has not been explored. Another largely unexplored aspect is edge effects, as most studies mentioned above deal with drops moving far away from the cell boundaries.

In this article, we make a connection between regular sessile drops and flattened confined drops and show that there exists a quasi-two-dimensional (Q2D) analogy for the widely studied three-dimensional (3D) sessile drops on non-wetting surfaces. The analogy is based on confining liquid in a vertical Hele-Shaw cell, forming a thin capillary bridge that is supported by the Hele-Shaw cell edge and deformed by gravity. We show that these flat and deformed vertical capillary bridges behave surprisingly similarly to 3D drops, showing analogous static and dynamic behaviors under a variety of external driving fields including gravity, shear, and electric and magnetic fields[28].

Results

Formation of stationary Q2D liquid drops

The formation of an ideal Q2D drop requires a sample cell (Hele-Shaw cell) consisting of two rigid transparent substrates with a uniform gap between them. To achieve sufficient uniformity, we used 4 mm thick optical grade

Department of Applied Physics, Aalto University School of Science, Puumiehenkuja 2, 02150 Espoo, Finland. e-mail: jaakko.timonen@aalto.fi

glass windows with $\lambda/4$ flatness (i.e. vertical distance between peaks and valleys on the window less than $\lambda/4 \sim 160$ nm, $\lambda = 633$ nm). The optical windows were thoroughly cleaned to suppress contact angle hysteresis and pinning, and assembled together using plastic spacers and metal clips under HEPA filtered air to achieve an essentially dust free cell with a gap $b \sim 100$ μm between the confining surfaces (see "Methods" for details). While Q2D drops can be, in principle, prepared in a cell with any gap smaller than the capillary length, we chose to work close to $b \sim 100$ μm as therein the gravitational force ($F_g \propto Ab$, where A is the projected area of the Q2D drop) is large enough to overcome the remaining (minor) contact line force ($F_{CL} \propto \sqrt{A}$). This enables close to ideal equilibrium drop shapes, i.e. shapes that are solely determined by the balance between hydrostatic pressure and Laplace pressure. Another reason to work with cells with $b \sim 100$ μm is that in thinner cells the non-uniformity of b becomes more critical as Laplace pressure ($\Delta p = 2\gamma/b$) gradients become more prominent. For example, 1 μm deviation over 1 cm distance in a cell with average thickness of $b = 30$ μm leads to pressure gradient of ca. 100 Pa cm^{-1} with typical fluids, which can easily distort the confined drops[16]. The cell thickness was quantified by measuring at multiple points using white light interferometry for each constructed cell (Supplementary Note 1, Supplementary Fig. 1, Supplementary Table 1) with typical non-uniformity of $\Delta b \sim 1$ μm within the multicentimetre-sized cell.

The resemblance between the traditional 3D sessile drops (Fig. 1a) and the Q2D drops (Fig. 1b) is obvious. The resemblance is valid for both small and large drop sizes (Supplementary Fig. 2). While the 3D drops appear mostly dark, Q2D drops are uniformly transparent with only a narrow dark band near the edge of the drop. In the 3D drops, the nearly entirely dark appearance is caused by refraction of the background light from the curved liquid-air interface (Fig. 1c). In contrast, refraction in the Q2D drops is present only near the drop edges with concave meniscus (Fig. 1d, Supplementary Fig. 3), leading to overall even passage of light through the drop. With approximately collimated illumination and low numerical aperture imaging, the expected width of the dark boundary is ca. $b/2$, as observed experimentally (Supplementary Fig. 3). The settled down Q2D drops appear to be sitting on a dark substrate (Fig. 1b), which does not reflect light as in the case of 3D drops to create a mirror image of the drop (Fig. 1a). This is because the apparent surface is not a real surface, but rather a pseudo-surface that arises from refraction of light from the 45°-angled edge of the glass window (Fig. 1d, Supplementary Fig. 4).

A theoretical model describing the equilibrium shape of Q2D pseudo-sessile drops can be derived by modifying the widely used model for 3D drops[1,29–31]. The model describes local drop half-width x as a function of distance z starting from the drop apex (Fig. 1e). Starting from hydrostatic pressure $p(z) = \rho g z$ (where ρ is liquid density and g is gravitational acceleration) and Laplace pressure $\Delta p = \gamma(\frac{1}{R_1} + \frac{1}{R_2})$ (where γ is surface tension and R_1 and R_2 are the two principal radii of curvature), the governing equation for the Q2D drop shape can be derived to be (Supplementary

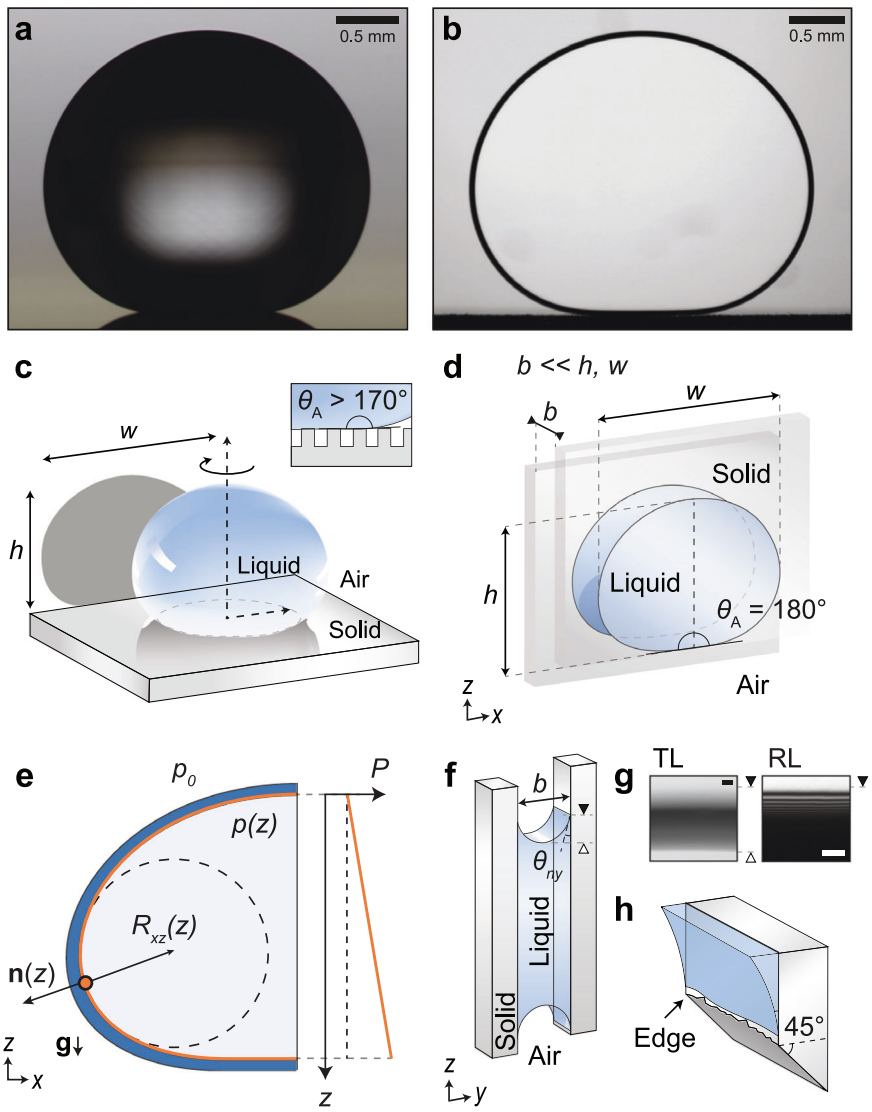

Fig. 1 | Quasi-two-dimensional (Q2D) pseudo-sessile drops resemble three-dimensional (3D) sessile drops on non-wetting surfaces. a An image of a 3D sessile water drop on a superhydrophobic surface based on micropillars and low surface energy coating. Image kindly provided by Sakari Lepikko. **b** An image of a Q2D pseudo-sessile water drop on a non-wetting pseudo-surface formed between two wetting glass windows ($b \simeq 120$ μm). **c** A scheme corresponding to the axisymmetric 3D drop in (**a**) with a large apparent contact angle (θ_A). The inset shows the micropillar structure of the substrate. **d** A scheme corresponding to the Q2D drop in (**b**) viewed from the front. The Q2D drop has an apparent contact angle of perfect 180°. b is cell thickness, h and w are drop height and width, respectively. **e** The model geometry for the equilibrium shape of the Q2D pseudo-sessile drops. p_0 and $p(z)$ is pressure outside and inside the drop, respectively. n(z) is the normal vector at the mid-plane of the sample cell and $R_{xz}(z)$ is local radius of curvature. The gravity vector g shows the direction of gravitational acceleration. **f** A scheme corresponding to the Q2D drop in (**b**) viewed from the side, where real contact angle $\theta \approx 0°$. **g** Transmitted and reflected light (TL, RL, respectively) microscopy images of the Q2D drop meniscus where interference fringes arise from the thin liquid wedge. Scale bars are 10 μm. **h** A scheme corresponding to the edge of the optical window where the liquid wedge meets 45°-angled corner of the glass window.

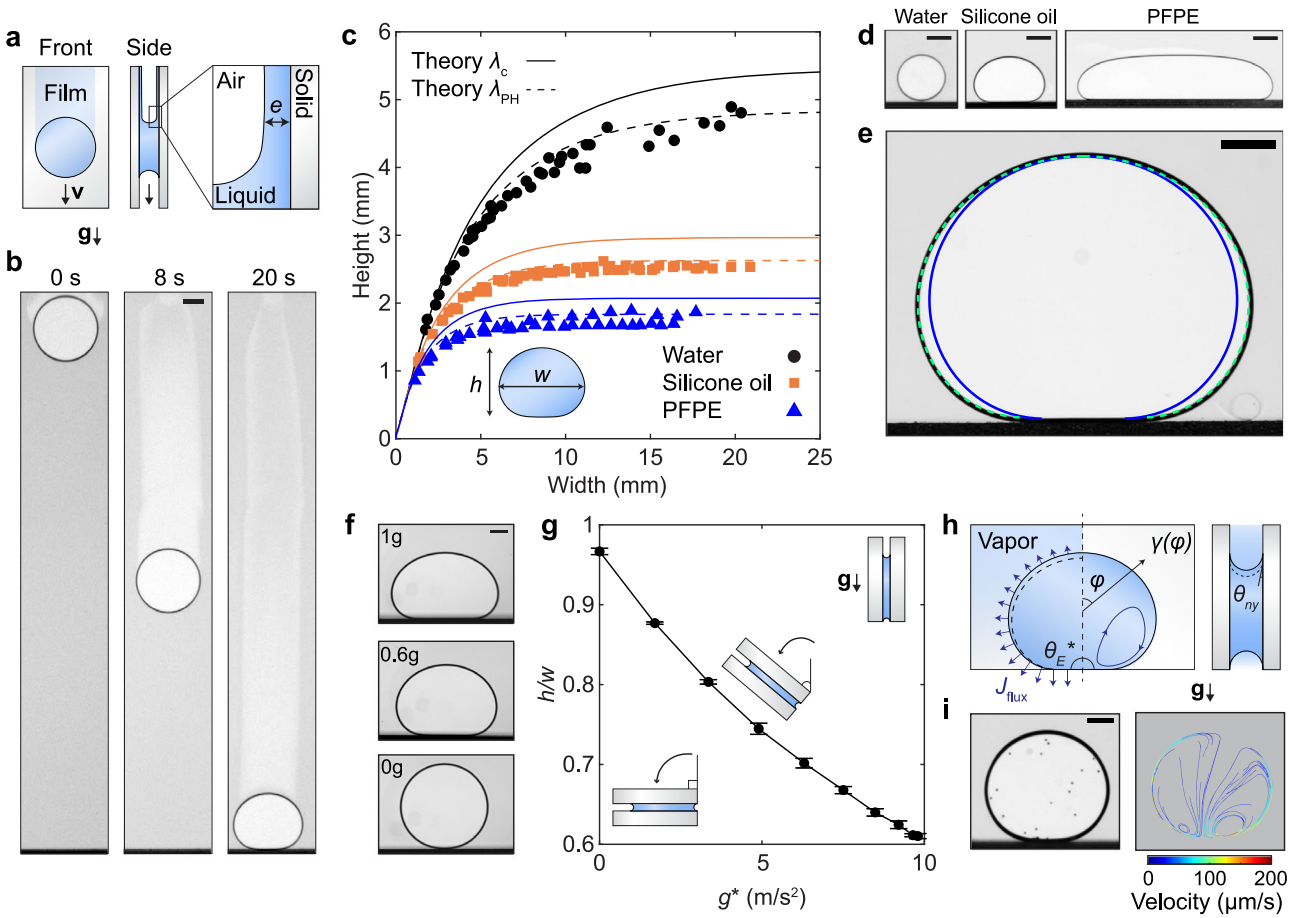

Fig. 2 | Equilibrium shapes, falling and evaporation of Q2D pseudo-sessile drops. **a** A scheme showing front and side profiles of a falling Q2D drop that leaves a residual film on the glass surfaces. Close-up shows the receding part of a falling Q2D drop, where a liquid film of thickness e is indicated. **b** Time series of a falling Q2D water drop ($b \simeq 120$ μm). Scale bar is 1 mm. **c** Height h of the Q2D pseudo-sessile drops as a function drop width w. Black circles, orange squares, and blue triangles represent experimental data for water, silicone oil and PFPE, respectively. Solid and dashed lines are theoretical fits using capillary length (λ_c) and effective capillary length (λ_{PH}), respectively. **d** Images of water, silicone oil and PFPE Q2D pseudo-sessile drops of same height (1.7 mm). All scale bars are 1 mm. **e** An image of a Q2D pseudo-sessile water drop overlayed with theoretical fits using $\lambda_c = 2.73$ mm (solid blue line) and $\lambda_{PH} = 2.26$ mm (dashed green line). Scale bar is 0.5 mm. **f** Images of a Q2D pseudo-sessile silicone oil drop under effective gravity of 9.8 m s^{-2}, 6.0 and 0.0 m s^{-2}. **g** Q2D silicone oil drop aspect ratio h/w as a function of effective gravity. Error bars indicate standard deviation calculated from three experiments. **h** Schemes for an evaporating Q2D drop viewed from the front and the side. Higher evaporative flux at the open sample cell bottom induces non-uniform surface tension $\gamma(\varphi)$ that drive Marangoni flows. **i** An image of a Q2D water drop with polyethylene particles and corresponding time-lapse particle trajectories and their velocities measured during 2.5 min time span. Scale bar is 0.5 mm.

Note 2).

$$p(z) - p_0 = \gamma\left(\frac{1}{R_{xz(z)}} + \frac{1}{R_{ny}}\right) \quad (1)$$

where $\frac{1}{R_{xz(z)}} = \nabla\hat{\boldsymbol{n}} = \frac{x_{zz}}{(1+x_z^2)^{\frac{3}{2}}}$, where $x_z = \frac{dx}{dz}$ and $x_{zz} = \frac{d^2x}{dz^2}$. The main difference compared to the analogous governing equation for the 3D sessile drops is the slightly different curvature term, which has a minor effect on the drop's projected shape (Supplementary Fig. 5). However, both the 3D and Q2D governing equations contain the same characteristic length scale, the capillary length $\lambda_c = \sqrt{\frac{\gamma}{\rho g}}$. Equation (1) can be numerically solved to obtain $x(z)$, from which the drop width w, height h, and projected area A can be extracted and compared to the experiments (Supplementary Note 3). In all simulations, perfect wetting with 0° local CA and hemispherical meniscus is assumed everywhere along the drop boundary (Fig. 1f). For Q2D water drops, the true contact angle was confirmed to be <3° using confocal reflection interference contrast microscopy, as expected for water on clean glass (Fig. 1g, Supplementary Note 4, Supplementary Fig. 6). We also confirmed the radius of curvature R_{ny} of the Q2D drops to be ~ 2/b, with slight asymmetry between drop apex and bottom (Supplementary Fig. 3d, e).

It is important to note that the pseudo-surface is an edge effect at the three-phase contact line that allows the Q2D drops to remain stationary at the edge of the optical window. Ideally, the weight of the Q2D drop is supported by the edge of the optical window (Fig. 1h), but other physico-chemical features such as impurities on the glass surface, can induce force that supports the weight of the Q2D drop and leads to drops sitting above the edge (Supplementary Fig. 4). Thus, the physical and chemical properties of the glass surface near the edge are important, and any microscale structures and impurities may cause deformation and pinning of the contact line (Supplementary Fig. 4).

Equilibrium shape, falling dynamics and evaporation of Q2D drops

The Q2D drops can be pipetted into the Hele-Shaw cell either from the bottom or top. In the latter case, the Q2D drop falls within the confinement (Supplementary Movie 1, Fig. 2a, b) analogously to 3D drops falling in air[32]. However, in contrast to the falling 3D drops, the terminal velocities of typical falling Q2D water drops with volume $V \sim 1$ μl are orders of magnitude slower (~ 10^{-3} m s^{-1}) and the Q2D drops leave behind a thin liquid

film of thickness e (Fig. 2a, b). This is similar to liquid slugs moving in capillaries[33,34]. Moving Q2D drops hence lose volume, which can be quantified from the size change of the drops. For example, for a falling water drop (Fig. 2b, $A \approx 7\ \mathrm{mm}^2$, $v = 1.5\ \mathrm{mm\ s^{-1}}$) the rate of volume loss is $Q \sim 2\ \mathrm{nl\ s^{-1}}$, which converts to an average trailing film thickness $e = \frac{\sqrt{\pi}Q}{4v\sqrt{A}} = 230\ \mathrm{nm}$. This is in approximative agreement with Landau-Levich-Derjaguin model predicting $e \approx b\mathrm{Ca}^{2/3} \approx 90\ \mathrm{nm}$, $\mathrm{Ca} = \eta v/\gamma$ is capillary number, η is viscosity, v is drop velocity and γ is surface tension[35,36]. As the film thickness is on the order of wavelength of light, direct measurement of the deposited film thickness is possible with e.g. optical interferometry, as suggested by the intensity variations within the trailing film (Fig. 2b).

The slower falling velocity compared to 3D drops is caused by the significantly larger viscous dissipation due to the confinement and the no-slip boundary condition. Because the kinetic energy is very modest in Q2D drops, the impact is also much gentler (Supplementary Movie 1)[37,38]. This is also apparent when comparing Weber numbers $\mathrm{We} = \rho v^2 L/\gamma$ of millimetric 3D and Q2D water drops released at a height of 3 cm: Just before drop impacting the surface the Weber number of a 3D drop is $\mathrm{We} \approx 9$, while for a Q2D drop $\mathrm{We} \approx 5 \times 10^{-5}$ ($v_{3D} = 0.8\ \mathrm{m\ s^{-1}}$, $v_{\mathrm{Q2D}} = 0.002\ \mathrm{m\ s^{-1}}$, $L_{3\mathrm{D}} = L_{\mathrm{Q2D}} = R$). After the impact, the Q2D drops adopt the equilibrium shape as described earlier within few seconds and remain stationary thereafter (Fig. 2b, Supplementary Movie 1).

The equilibrium shapes of the Q2D pseudo-sessile drops were examined as a function of drop volume for three liquids with different capillary lengths: water ($\lambda_c = 2.7\ \mathrm{mm}$), silicone oil ($\lambda_c = 1.5\ \mathrm{mm}$) and perfluoropolyether (PFPE, $\lambda_c = 1.0\ \mathrm{mm}$) (Supplementary Table 2). For all studied liquids, both the drop height and width increased monotonically with the increasing drop volume (Fig. 2c). As with 3D drops, the Q2D drops became gradually deformed by gravity with increasing drop volume and decreasing capillary length (Fig. 2d, Supplementary Fig. 2). The Q2D drop heights saturated for all liquids at large volume limit, analogous to the puddle limit known for 3D drops. At the Q2D puddle limit, the puddle heights were 4.70 mm, 2.55 mm and 1.75 mm for water, silicone oil and PFPE, respectively (Fig. 2c).

Comparison between the theoretically predicted drop shapes (Eq. (1)) and the experimental ones was done by overlaying the predicted shape from the model onto the experimental images and adjusting the apex curvature κ_0 to match the experimentally observed drop height (Fig. 2e). We noticed that the experimentally observed drop shapes were systematically slightly wider than those predicted theoretically, especially at the Q2D puddle limit, at which the theory predicts the puddle height to be $2\lambda_c$ (Fig. 2c, d). This can be explained by the Park-Homsy correction[19,23,36,39] which is associated to the boundary conditions in the Hele-Shaw geometry when the liquid wets the solid surface and the aspect ratio b/R is small, as in our experiments, leading to effective capillary length $\lambda_{\mathrm{PH}} = \sqrt{\pi/4}\lambda_c$ (Fig. 2c).

In contrast to 3D drops, the Q2D geometry allows a convenient way to adjust the strength of the effective gravitational force acting on the Q2D drops. This is done by adjusting the component of the gravitational force along the Q2D drop plane by tilting the cell along the x-axis (Fig. 2f, g). Tilting enables the tangential component of the gravitational acceleration to be varied from $g^* \sim 0\ \mathrm{m\ s^{-2}}$ to $g^* \sim 9.81\ \mathrm{m\ s^{-2}}$, hence allowing one to control the effective gravity and observe a transition from gravity-deformed drops with aspect ratio $h/w < 1$ to perfectly circular drops with $h/w = 1$ (Fig. 2f, g). We note that analogous experiments with 3D drops would be considerably more challenging and require utilization of additional forces such as centrifugal force[40] or magnetic force[41], or controlled micro-gravity environment available in drop tower facilities[42,43], space[44,45] and zero-g flights[46].

The evaporation of Q2D drops is also expected to differ from the 3D counterparts because of the liquid drop shape and the boundary conditions. Using density-matched tracer particles, we observed a dipolar flow field inside a stationary and slowly evaporating water Q2D drop with $u \sim 10^{-4}\ \mathrm{m\ s^{-1}}$ peripheral flow along the drop surface, from the apex of the drop towards the bottom (Fig. 2h, i, Supplementary Movie 2). Countering flow at the middle of the drop upwards was also observed. This interfacial flow is likely driven by surface tension gradient arising from a temperature gradient caused by faster evaporation of water near the bottom of the drop exposed to ambient humidity compared to the drop apex being in equilibrium with saturated water vapor inside the Hele-Shaw cell. As Marangoni flow velocity scales as $u \sim (\Delta\gamma/\eta)(b/H)$[47,48], the magnitude of the surface tension difference between the bottom and the apex can be estimated to be $\sim 10^{-6}\ \mathrm{N\ m^{-1}}$. The corresponding temperature difference can be estimated to be $\Delta T = \frac{\Delta\gamma}{K} \sim 0.007\ ^\circ\mathrm{C}$, where $K = \frac{d\gamma}{dT} \approx -0.15\mathrm{mNm^{-1}\ ^\circ C^{-1}}$ near room temperature[49].

Sliding on tilted pseudo-surfaces

In addition to the falling dynamics and impacts, the Q2D drops can move laterally on the pseudo-surface when the cell is tilted (Fig. 3a). This is analogous to 3D drops moving on tilted surfaces, where the drop motion is driven by gravity and resisted by viscous and contact line forces[50–53]. We observed that the Q2D pseudo-sessile drops can start moving at very small tilting angles (Fig. 3b), indicating that contact line forces are small[54–57]. For example, the critical tilt angle (α_c) required to make a Q2D PFPE drop move was observed to be less than 0.5°. Analogous to 3D drops, where the terminal velocity scales as $\gamma \sin\alpha/\eta$ [3,16], the velocity of Q2D drops increases with $\sin\alpha$ (Fig. 3b) and decreases with increasing viscosity (Fig. 3c). The terminal velocity of Q2D drops arises from the balance between the tangential component of the gravitational force and the total viscous dissipation that can be divided into contribution arising from dissipation in the bulk of the drop and near the moving meniscus as

$$\pi R^2 b\rho g \sin\alpha = F_{\eta,\mathrm{bulk}} + F_{\eta,\mathrm{meniscus}} = 12\frac{\pi R^2}{b}\gamma\mathrm{Ca} + 4\pi R\beta\gamma\mathrm{Ca}^{2/3} \quad (2)$$

where $\beta = 3.5$ is a parameter linked to the geometry of the meniscus[16,58]. This model, without adjustable parameters for the fit, is consistent with our experimental data for moving pseudo-sessile Q2D PFPE drops for a wide range of drop volumes (from circular to puddle-like drops) and tilting angles (Fig. 3b). We also note that in typical Q2D drops, the viscous force near the moving meniscus dominates over viscous force in the bulk since $F_{\eta,\mathrm{bulk}} < F_{\eta,\mathrm{meniscus}}$ when $\mathrm{Ca} < \left(\frac{\beta b}{3R}\right)^3 \sim 10^{-3}$, valid in our experiments (Fig. 3b). Even at higher capillary numbers (such as $\mathrm{Ca} \sim 0.3 \times 10^{-3}$, 1 µl PFPE Q2D drop moving at 0.4 mm s^{-1}, $\beta = 20°$), the total viscous force of 6.7 µN is dominated by the meniscus component (4.9 µN) over the bulk component (1.8 µN).

Finally, we analysed the flow fields inside moving Q2D pseudo-sessile drops using tracer particles. In contrast to large CA 3D drops that can move by sliding or rolling[52,59,60], the Q2D drops appear to move solely by sliding. This is caused by the vertical no-slip boundaries at the two sides of the drop. As Reynolds number $\mathrm{Re} = \rho v L/\eta$ in moving Q2D drops is small (e.g. $\mathrm{Re} \approx 0.2$ for a Q2D water drop sliding with 1 mm s^{-1} velocity when $L = 220\ \mu\mathrm{m}$), the flow is laminar and parabolic between these two confining surfaces (Fig. 3d). This was investigated using silicone oil Q2D drops containing polyethylene particles. The drop ($V \sim 2$ µl) moving with a velocity of ~0.1 mm s^{-1} ($\mathrm{Re} < 10^{-3}$) was observed to contain particles moving at velocities ranging from 0 mm s^{-1} to 0.23 mm s^{-1} with highest concentration of particles moving at 0.15 mm s^{-1} which is close to the mean velocity (Fig. 3e). The experiments with tracer particles also revealed, unexpectedly, more complex behaviors for moving Q2D water drops, where backwards directed flow near the perimeter of the drop was observed (Supplementary Movie 3, Fig. 3f). This contrasts with the silicone oil experiments where such backwards flows were absent. The mean velocities of Q2D water drops were also observed to be notably smaller (up to 80% smaller) than expected based on viscous dissipation only (Fig. 3g). This suggests a presence of additional friction forces in Q2D water drops, likely acting on the contact line.

More complex phenomena: levitation, magnetic instabilities and electrohydrodynamic structuring

Finally, we tested whether other, more complex, phenomena seen in 3D sessile drops driven by shear[9,10,61], magnetic fields[62–64] and electric fields[65] can

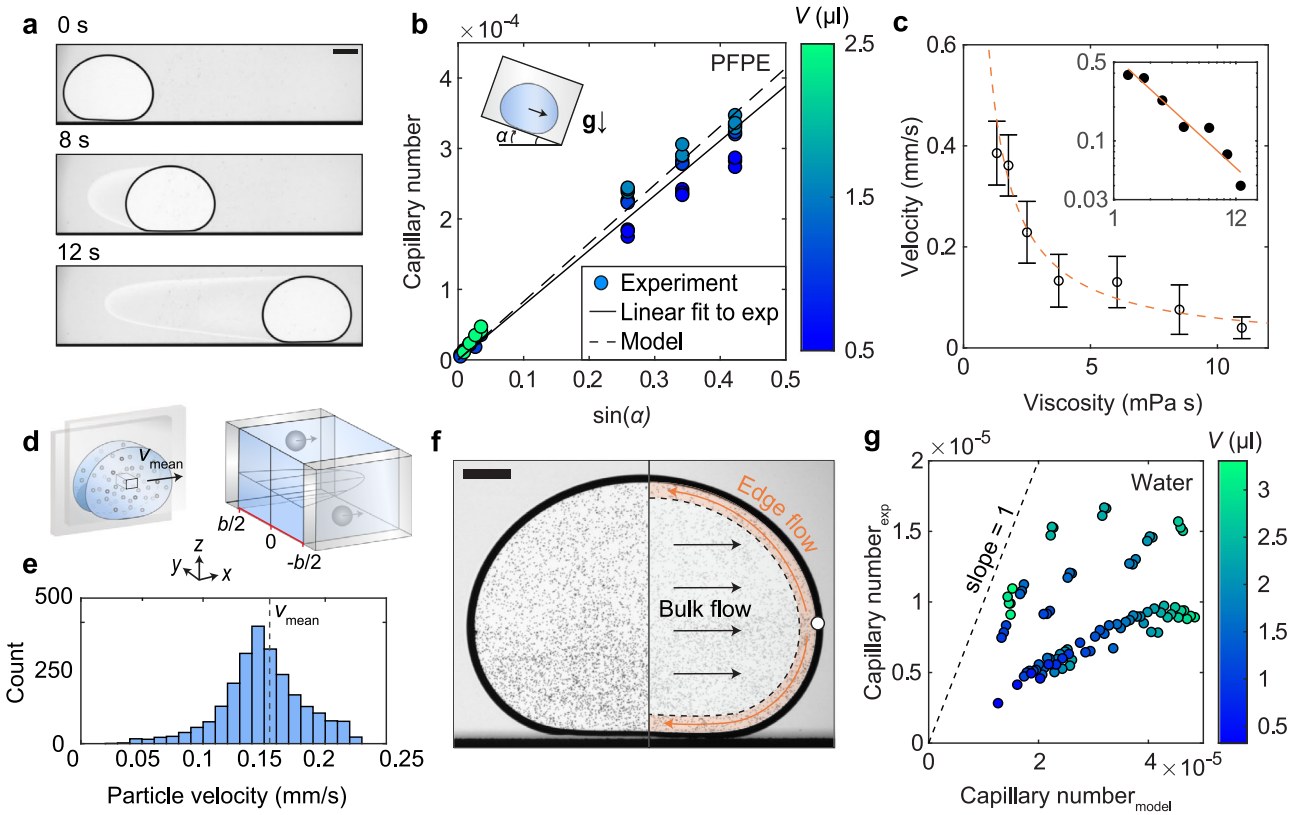

Fig. 3 | Q2D drops moving on tilted pseudo-surfaces. a Time series of a Q2D water drop moving on a pseudo-surface (α = 15°, scale bar is 1 mm). **b** Capillary number (Ca) as a function of sin α for Q2D PFPE drops. Filled circles correspond to experimental data, and solid and dashed lines are linear fits to the experimental data and the theoretical model, respectively. Drop volume is indicated by the colormap. **c** Q2D drop velocity as a function of drop viscosity for water-glycerol mixtures (V ~ 1.5 μl, α = 10°). Circles correspond to experimental mean velocities from 5 to 23 drops each. Error bars indicate the standard deviation. Dashed orange line corresponds to best fit of $v \propto 1/\eta$. The inset shows the same data in a log-log plot. **d** A scheme of a laterally moving Q2D drop containing tracer particles and a magnified view of the expected flow field. **e** Velocity histogram of measured particle velocities in laterally moving Q2D silicone oil drop. **f** A snapshot of a moving Q2D pseudo-sessile water drop with polystyrene particles (Supplementary Movie 3) and a simplified overlayed scheme of the observed flow patterns: Bulk flow towards the direction of motion (black arrows) and countering edge flows (orange arrows). The white circle indicates a stagnation point. Scale bar is 0.5 mm. **g** Experimental Ca as a function of model Ca for water Q2D drops with α varying between 10° and 25° (b ≃ 220 μm for **a**–**g**).

be seen in Q2D drops. Firstly, 3D drops moving relative to the surrounding gas phase are known to experience shear force that can lead to complex drop shapes, fragmentation and even levitation[32,66–70]. Analogously in Q2D drops, aerodynamic lift and apparent levitation can be achieved by overcoming the gravitational force F_G with aerodynamic drag force F_D using upwards flowing gas in the Hele-Shaw cell (Fig. 4a, b, Supplementary Movie 4). The gas flow was introduced by a hand-held nitrogen gun with approximate nozzle size of 5 mm. When the size of the drop was larger than the nozzle diameter, the levitating drops fragmented into two separated Q2D drops (Supplementary Movie 5, Fig. 4c). This is analogous to the falling large 3D drops that disintegrate during the fall, limiting for example the size of the raindrops falling from the sky[32,66,67].

Secondly, 3D drops of magnetic liquids have been known since the 1960s to exhibit a variety of deformations and pattern formation in magnetic fields driven by reduction in magnetostatic energy[63,64,71], also in Hele-Shaw geometry as large pools[72,73]. Similarly, Q2D droplets made of a strongly magnetic colloidal dispersion, a ferrofluid, are expected to deform in an external magnetic field (Fig. 4d). Indeed, when a magnetizable Q2D drop was subjected to a non-uniform magnetic field from a permanent magnet below the Q2D drop, we observed deformation of the drop followed by instability on the drop surface reminiscent of the well-known Rosensweig instability[62–64] (Fig. 4e, f, Supplementary Movie 6).

Thirdly, 3D drops are known to undergo a plethora of non-equilibrium phenomena when subjected to electric fields that cause electrohydrodynamic forces[74–77]. Similarly, we observed that a Q2D drop of insulating perfluoropolyether (PFPE, $\sigma_{PFPE} \sim 10^{-17}$ S m^{-1}) surrounded by a slightly conductive mixture of Aerosol OT and dodecane ($\sigma_{AOT-DD} \sim 10^{-8}$ S m^{-1}) [65] confined between transparent indium tin oxide (ITO) coated glass slides providing perpendicular electric field[65,78] can undergo complex electrohydrodynamically driven structuring (Fig. 4g, h, Supplementary Movie 7).

Conclusions

We have realized pseudo-sessile quasi-two-dimensional (Q2D) liquid drops with large apparent contact angles as an analogy for the widely studied three-dimensional (3D) drops on non-wetting surfaces. Although the analogy between 3D drops and Q2D drops is a macroscopic interpretation, many of the static and dynamic behaviors of the Q2D drops in gravitational, shear, electric and magnetic field are conceptually analogous to those of the conventional 3D drops studied on superhydrophobic surfaces[2,4–6,8,53,79], superoleophobic surfaces[80,81], Leidenfrost states[9,10,82] and as fizzy drops[12,13]. While in this demonstration we focused on surfaces wetted by the studied liquids ($\theta \sim 0°$), larger contact angles can be also possible – for example ca. $\theta \sim 90°$ using slippery-omniphobic covalently attached liquid (SOCAL) surfaces[83], or close to $\theta \sim 180°$ with superhydrophobic surfaces[84].

Our work expands the previous studies on statics and dynamics of flat capillary bridges[14,26,27] to situations where the bridge is resting on a pseudo-surface, an edge effect, leading to a gravity-deformed bridge. We also approach the 2D limit by reducing the Hele-Shaw cell thickness by one order of magnitude (from ~ 1 mm to ~ 0.1 mm). The main challenge for creating and studying high quality pseudo-sessile Q2D drops is in the sample cell

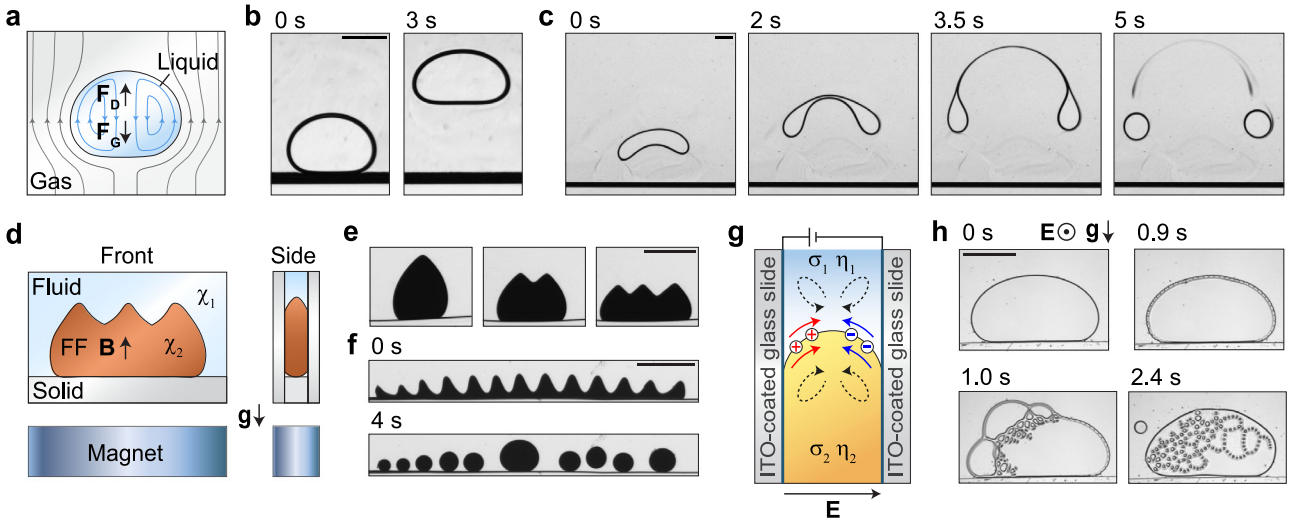

Fig. 4 | Levitation, magnetic instabilities and electrohydrodynamic structuring of Q2D pseudo-sessile drops. a Schematic front view of a Q2D drop levitating under in-plane gas flow, where F_G is gravitational force and F_D is aerodynamic drag force. **b** Time series of a small Q2D PFPE drop levitating under planar nitrogen flow ($V \sim 0.5$ µl; $b \simeq 220$ µm). **c** Time series of a larger Q2D PFPE drop levitating and splitting under planar flow (initial drop $V \sim 1$ µl; $b \simeq 220$ µm). **d** Schematic front and side views of a magnetizable Q2D drop (FF = ferrofluid) undergoing instabilities in applied nonhomogeneous magnetic field (B) created by a permanent magnet under the Hele-Shaw cell. χ_i is the magnetic susceptibility for the two fluids. **e** Three microscopy images showing a magnetizable fluorocarbon based Q2D drop surrounded by solution of dodecane containing Aerosol OT surfactant in three states of increasing magnetic field strength ($V \sim 0.03$ µl; $b \sim 60$ µm). **f** Time series of the magnetizable Q2D drop undergoing instabilities that result in splitting of the drop ($V \sim 0.05$ µl; $b \sim 60$ µm). **g** Schematic side view of the interface between a Q2D drop and a surrounding liquid in an electric field (E). σ_i and η_i are conductivity and viscosity for the two fluids, respectively. **h** Time series of microscopy images of a PFPE Q2D drop undergoing electrohydrodynamically driven structuring ($V \sim 0.05$ µl; $b \sim 60$ µm). All scale bars are 1 mm.

preparation: a Hele-Shaw cell with very small contact angle hysteresis and uniform cell thickness is required. Another important feature is that, because of strong viscous dissipation, dynamic phenomena such as drop impacts are more subtle than in 3D. On the other hand, the excellent optical access to the droplet contents (relevant for e.g. drops of colloidal dispersions), convenient ability to add and tune external fields (such as gravity and electric field) and the possibility of observing phenomena arising from the reduced dimensionality and boundary conditions, e.g. the edge effect, are likely to lead to discovery of various capillary phenomena not possible in conventional 3D drops.

Methods

Materials

Sample cells. Optical windows (Edmund Optics 47-944, uncoated square borosilicate-crown glass, 50 mm × 50 mm, $\lambda/4$ surface flatness), glass slides (VWR 631-1552), indium tin oxide (ITO) coated glass slides (Diamonds Coatings Ltd., nominal thickness of coating ~ 350 nm), lens cleaning tissues (Thorlabs MC-50E), plastic spacers (PrecisionBrand plastic shim set 77-644-905), thermoplastic Surlyn ionomer film (DuPont 1702) and office clippers.

Liquids. Ethanol (Altia 1025874), silicone oil (Sigma-Aldrich 317667), perfluoropolyether (Chemours Performance Lubricants GPL 102-500), glycerol (Fisher BioReagents BP2291) and ferrofluid (Ferrotec DFF2, lot. T041019A) were used as received. De-ionized (DI) water (MerckMillipore Direct-Q® 3 UV Water Purification System ZRQSVP3WW) was filtered (Fisher 15206869, 17144381, 0.2–0.45 µm pore size) before experiments. See Supplementary Table 2 for details. 150 mM docusate sodium salt (AOT) solution in *n*-dodecane was prepared by dissolving AOT (Sigma-Aldrich, 99%) in *n*-dodecane (Acros Organics, 99%, anhydrous).

Particles. Grey polyethylene (PE) microspheres (Cospheric GRYPMS-1.00, density 1.00 g cc^{-1}, diameter distribution 10–45 µm) and polystyrene microparticles (MicroParticles GmbH PS/Q-R-KM544, 10 µm) were either used as received and washed by centrifugation, respectively. The density-matching of the PE particles was done by centrifugation, followed by discarding the sedimented and creamed particles as done before[85]. Further, the particle dispersion was left to sediment/cream overnight, after which the particle dispersion from the middle part of the container was used in the experiments.

Methods

All experiments were performed under ambient laboratory conditions.

Preparation of Q2D sample cells. Optical glass windows were cleaned by pipetting a ca. 50 µl solvent drop on the glass surface, placing a lens cleaning tissue on the drop and dragging the wet tissue slowly on the surface, leaving behind a dry surface. This was done first with DI water and then with ethanol, ca. three times in different directions with both liquids. Additionally, optical window edges were cleaned with ethanol-wetted cotton swabs. Lastly the windows were rinsed with DI water and dried with a nitrogen gun. Subsequently, the optical windows were plasma activated (Henniker Scientific Ltd. HPT-100, air plasma, 80% power, 3 minutes), and the cell was assembled in a HEPA-filtered biological safety cabinet (Kojair Biowizard Golden Line) using nominally 102 or 191 µm thick and 1–2 cm wide plastic spacers that were wiped with ethanol and dried before sandwiching them between the optical windows. Finally, the optical windows and spacers were clamped together with office clippers. The sample cell was protected from airborne dust at all times when possible. Just prior to the experiments, a nitrogen gun was used to remove any accumulated dust from the cell.

Optical imaging. Custom imaging setups consisted of a 0.16x or 1x objective (Edmund Optics 56-675, Mitutoyo 378-800-3) coupled either directly, or via tube lens (Thorlabs), to a USB-camera (Ximea MC050CG-SY, Basler 35-927, FLIR GS3-U3-51S5M-C). The light source in the custom setups was either a LED panel (Godox LEDP120C) or collimated LED (Thorlabs MWWHLP1 with SM2F32-A). Additional imaging was done with a commercial goniometer (Biolin Scientific Attension Theta).

Preparation and manipulation of Q2D drops. The Q2D sample cell was placed on a sample stage composed of a plate holder (Thorlabs FP02)

mounted to a tilting stage (Thorlabs GNL10/M) and xyz-translation stage (Thorlabs PT3/M). The tilting stage was used to align the sample cell normal to gravity. Experiments started with a small liquid volume (0.5–1 μl) pipetted into the sample cell, followed by drop size being increased stepwise by adding ~ 0.5–1 μl of the liquid and acquiring a new image after each addition. The effect of the tangential component of the gravity on the equilibrium shape of the Q2D drop was studied by placing the Q2D sample cell in a cage system (Thorlabs) mounted on a goniometer stage (Thorlabs NR360S/M) that allowed the tilting of the sample cell 0–90° with respect to the horizon. On the other hand, to observe falling Q2D drops, the liquid ($V \sim 1$ μl) was pipetted in a single step from the top of the sample cell and the falling of the Q2D drop was recorded. Finally, drop sliding experiments were done with a custom setup consisting of a tilting stage (Thorlabs GNL10/M) for tilt angles $\alpha \leq 10°$, and using a commercial goniometer (Biolin Scientific Attension Theta) for tilt angles $\alpha > 10°$.

Levitation, magnetic instabilities and electrohydrodynamic structuring in Q2D drops. For Q2D drop levitation experiments, the sample cell was constructed from optical windows as in '*Preparation of Q2D sample cells*'. A Q2D PFPE drop in the bottom of a vertical sample cell was exposed to gas flow with a manually operated nitrogen gun positioned below the sample cell. The ferrofluid and EHD experiments were done in Hele-Shaw cells constructed using indium tin oxide coated glass slides[65,78]. The cell was first filled with dodecane containing 150 mM AOT (leaving some room for the Q2D drop), and then, either ferrofluid or PFPE was pipetted inside the sample cell creating a Q2D drop that was let to sediment on the bottom of the vertical sealed sample cell. In the ferrofluid Q2D drop experiments, a permanent cylindrical NdFeB magnet (1" diameter, 1" height, K&J Magnetics DX0×0-N52) was slowly moved beneath the sample cell. The distance between the bottom of the ferrofluid drop and magnet varied from 5 mm ($B \sim 0.3$ T) to 15 cm ($B \simeq 0$ T). In the EHD experiments, an electrometer (Keysight B2987A) was connected to the ITO-coated glass sample cell with wires (Alpha Wire 2936), and a DC electric field of magnitude of 4.14 V μm^{-1} was applied for 250 ms and then lowered to 3.5 V μm^{-1} until the electric field was switched off after ~ 10 s.

Measurement of Q2D drop dimensions, area, and position. Drop height (h) and width (w) were measured from the inner edges of the Q2D drops using the FIJI/ImageJ profile plot tool[86,87]. A custom MATLAB script was used to detect the boundaries of the Q2D drops and thus obtain the drop profile $x(z)$, area A and volume $V = Ab$. The position of a moving Q2D drop was measured with a custom MATLAB script.

Tracking and measurement of particle velocities in Q2D drops. The experimental videos were cropped with moving region of interest using a custom MATLAB code and processed (threshold, binarization) prior to analysis performed with FIJI/ImageJ plug-in TrackMate[88,89].

Data availability

All data are available in the main text or the supplementary materials. Numerical data is provided in Supplementary Data 1. High resolution image and video data is available from the corresponding author upon reasonable request.

Received: 6 March 2024; Accepted: 4 October 2024;
Published online: 14 October 2024

References

1. De Gennes, P.G., Brochard- Wyart, F. & Quéré, D. *Capillarity and Wetting Phenomena: Drops, Bubbles, Pearls, Waves* (Springer, New York, NY, translation of the French ed., 2010).
2. Lafuma, A. & Quéré, D. Superhydrophobic states. *Nat. Mater.* **2**, 457–460 (2003).
3. Mouterde, T., Raux, P. S., Clanet, C. & Quéré, D. Superhydrophobic frictions. *Proc. Natl. Acad. Sci. USA* **116**, 8220–8223 (2019).
4. Wang, D. et al. Design of robust superhydrophobic surfaces. *Nature* **582**, 55–59 (2020).
5. Quéré, D. & Reyssat, M. Non-adhesive lotus and other hydrophobic materials. *Philos. Trans. R. Soc. A.* **366**, 1539–1556 (2008).
6. Tian, X., Verho, T. & Ras, R. H. A. Moving superhydrophobic surfaces toward real-world applications. *Science* **352**, 142–143 (2016).
7. Cassie, A. B. D. & Baxter, S. Wettability of porous surfaces. *Trans. Faraday Soc.* **40**, 546 (1944).
8. Quéré, D. Wetting and roughness. *Annu. Rev. Mater. Res.* **38**, 71–99 (2008).
9. Biance, A.-L., Clanet, C. & Quéré, D. Leidenfrost drops. *Phys. Fluids* **15**, 1632 (2003).
10. Quéré, D. Leidenfrost dynamics. *Annu. Rev. Fluid Mech.* **45**, 197–215 (2013).
11. Neitzel, G. P. & Dell'Aversana, P. Noncolaescence and nonwetting behavior of liquds. *Annu. Rev. Fluid Mech.* **34**, 267–289 (2002).
12. Panchanathan, D. et al. Levitation of fizzy drops. *Sci. Adv.* **7**, eabf0888 (2021).
13. Backholm, M. et al. Toward vanishing droplet friction on repellent surfaces. *Proc. Natl. Acad. Sci. USA* **121**, e2315214121 (2024).
14. Okumura, K. Viscous dynamics of drops and bubbles in Hele-Shaw cells: Drainage, drag friction, coalescence, and bursting. *Adv. Colloid Interface Sci.* **255**, 64–75 (2018).
15. Hele-Shaw, H. S. The flow of water. *Nature* **58**, 34–36 (1898).
16. Reyssat, E. Drops and bubbles in wedges. *J. Fluid Mech.* **748**, 641–662 (2014).
17. Yokota, M. & Okumura, K. Dimensional crossover in the coalescence dynamics of viscous drops confined in between two plates. *Proc. Natl Acad. Sci. USA* **108**, 6395–6398 (2011).
18. Dangla, R., Lee, S. & Baroud, C. N. Trapping microfluidic drops in wells of surface energy. *Phys. Rev. Lett.* **107**, 124501 (2011).
19. Nagel, M., Brun, P.-T. & Gallaire, F. A numerical study of droplet trapping in microfluidic devices. *Phys. Fluids* **26**, 032002 (2014).
20. Marín, A. G., Enríquez, O. R., Brunet, P., Colinet, P. & Snoeijer, J. H. Universality of Tip Singularity Formation in Freezing Water Drops. *Phys. Rev. Lett.* **113**, 054301 (2014).
21. Schremb, M. & Tropea, C. Solidification of supercooled water in the vicinity of a solid wall. *Phys. Rev. E* **94**, 052804 (2016).
22. Chu, F. et al. Interfacial ice sprouting during salty water droplet freezing. *Nat. Commun.* **15**, 2249 (2024).
23. Reyssat, E. Capillary bridges between a plane and a cylindrical wall. *J. Fluid Mech.* **773**, R1 (2015).
24. Teh, S.-Y., Lin, R., Hung, L.-H. & Lee, A. P. Droplet microfluidics. *Lab Chip* **8**, 198 (2008).
25. Baroud, C. N., Gallaire, F. & Dangla, R. Dynamics of microfluidic droplets. *Lab Chip* **10**, 2032 (2010).
26. Tanaka, N. & Okumura, K. Viscous friction acting on a solid disk falling in confined fluid: Lessons for the scaling analysis. *Phys. Rev. Res.* **5**, L032047 (2023).
27. Daerr, A., Eggers, J., Limat, L. & Valade, N. General mechanism for the meandering instability of rivulets of newtonian fluids. *Phys. Rev. Lett.* **106**, 184501 (2011).
28. Li, X. et al. Kinetic drop friction. *Nat. Commun.* **14**, 4571 (2023).
29. Saad, S. M. I. & Neumann, A. W. Axisymmetric drop shape analysis (ADSA): An outline. *Adv. Colloid Interface Sci.* **238**, 62–87 (2016).
30. Adamson, A. W., Gast, A. P., *Physical Chemistry of Surfaces* (Wiley, New York, 6. ed., *A Wiley-Interscience publication*. 1997).
31. Dang, Q., Song, M., Luo, X., Qu, M. & Wang, X. A modeling study of different kinds of sessile droplets on the horizontal surface with surface wettability and gravity effects considered. *Energy Storage Sav.* **1**, 22–32 (2022).

32. Villermaux, E. & Bossa, B. Single-drop fragmentation determines size distribution of raindrops. *Nat. Phys.* **5**, 697–702 (2009).
33. Bico, J. & Quéré, D. Falling slugs. *J. Colloid Interface Sci.* **243**, 262–264 (2001).
34. Jensen, O. E. Draining collars and lenses in liquid-lined vertical tubes. *J. Colloid Interface Sci.* **221**, 38–49 (2000).
35. Bretherton, F. P. The motion of long bubbles in tubes. *J. Fluid Mech.* **10**, 166 (1961).
36. Park, C.-W. & Homsy, G. M. Two-phase displacement in Hele Shaw cells: Theory. *J. Fluid Mech.* **139**, 291–308 (1984).
37. Khojasteh, D., Kazerooni, M., Salarian, S. & Kamali, R. Droplet impact on superhydrophobic surfaces: A review of recent developments. *J. Ind. Eng. Chem.* **42**, 1–14 (2016).
38. Yarin, A. L. Drop impact dynamics: Splashing, spreading, receding, bouncing. *Annu. Rev. Fluid Mech.* **38**, 159–192 (2006).
39. Paterson, A., Fermigier, M., Jenffer, P. & Limat, L. Wetting on heterogeneous surfaces: Experiments in an imperfect Hele-Shaw cell. *Phys. Rev. E* **51**, 1291–1298 (1995).
40. Tadmor, R. et al. Measurement of lateral adhesion forces at the interface between a liquid drop and a substrate. *Phys. Rev. Lett.* **103**, 266101 (2009).
41. Timonen, J. V. I., Latikka, M., Ikkala, O. & Ras, R. H. A. Free-decay and resonant methods for investigating the fundamental limit of superhydrophobicity. *Nat. Commun.* **4**, 2398 (2013).
42. Diana, A., Castillo, M., Brutin, D. & Steinberg, T. Sessile drop wettability in normal and reduced gravity. *Microgravity Sci. Technol.* **24**, 195–202 (2012).
43. Zhu, Z.-Q. et al. Experimental investigation of pendant and sessile drops in microgravity. *Microgravity Sci. Technol.* **22**, 339–345 (2010).
44. Kumar, S., Medale, M., Marco, P. D. & Brutin, D. Sessile volatile drop evaporation under microgravity. *NPJ Microgravity* **6**, 37 (2020).
45. McCraney, J., Kern, V., Bostwick, J. B., Daniel, S. & Steen, P. H. Oscillations of drops with mobile contact lines on the international space station: Elucidation of terrestrial inertial droplet spreading. *Phys. Rev. Lett.* **129**, 084501 (2022).
46. Brutin, D. et al. Sessile drop in microgravity: Creation, contact angle and interface. *Microgravity Sci. Technol.* **21**, 67–76 (2009).
47. Nadim, A., Borhan, A. & Haj-Hariri, H. Tangential stress and marangoni effects at a fluid–fluid interface in a Hele–Shaw Cell. *J. Colloid Interface Sci.* **181**, 159–164 (1996).
48. Gallaire, F., Meliga, P., Laure, P. & Baroud, C. N. Marangoni induced force on a drop in a Hele Shaw cell. *Phys. Fluids* **26**, 062105 (2014).
49. Vargaftik, N. B., Volkov, B. N. & Voljak, L. D. International tables of the surface tension of water. *J. Phys. Chem. Ref. Data* **12**, 817–820 (1983).
50. Butt, H.-J. et al. Contact angle hysteresis. *Curr. Opin. Colloid Interface Sci.* **59**, 101574 (2022).
51. Olin, P., Lindström, S. B., Pettersson, T. & Wågberg, L. Water drop friction on superhydrophobic surfaces. *Langmuir* **29**, 9079–9089 (2013).
52. Yilbas, B. S., Al-Sharafi, A., Ali, H. & Al-Aqeeli, N. Dynamics of a water droplet on a hydrophobic inclined surface: influence of droplet size and surface inclination angle on droplet rolling. *RSC Adv.* **7**, 48806–48818 (2017).
53. Gao, N. et al. How drops start sliding over solid surfaces. *Nat. Phys.* **14**, 191–196 (2018).
54. Extrand, C. W. & Kumagai, Y. Liquid drops on an inclined plane: The relation between contact angles, drop shape, and retentive force. *J. Colloid Interface Sci.* **170**, 515–521 (1995).
55. Pilat, D. W. et al. Dynamic measurement of the force required to move a liquid drop on a solid surface. *Langmuir* **28**, 16812–16820 (2012).
56. ElSherbini, A. I. & Jacobi, A. M. Retention forces and contact angles for critical liquid drops on non-horizontal surfaces. *J. Colloid Interface Sci.* **299**, 841–849 (2006).
57. Backholm, M. et al. Water droplet friction and rolling dynamics on superhydrophobic surfaces. *Commun. Mater.* **1**, 64 (2020).
58. Cantat, I. Liquid meniscus friction on a wet plate: Bubbles, lamellae, and foams. *Phys. Fluids* **25**, 031303 (2013).
59. Mahadevan, L. & Pomeau, Y. Rolling droplets. *Phys. Fluids* **11**, 2449–2453 (1999).
60. Richard, D. & Quéré, D. Viscous drops rolling on a tilted non-wettable solid. *Europhys. Lett.* **48**, 286–291 (1999).
61. Graeber, G. et al. Leidenfrost droplet trampolining. *Nat. Commun.* **12**, 1727 (2021).
62. Rosensweig, R. E. *Ferrohydrodynamics* (Dover Publications, Inc, Mineola, New York, Dover edition., 2014).
63. Timonen, J. V. I., Latikka, M., Leibler, L., Ras, R. H. A. & Ikkala, O. Switchable static and dynamic self-assembly of magnetic droplets on superhydrophobic surfaces. *Science* **341**, 253–257 (2013).
64. Latikka, M. et al. Ferrofluid microdroplet splitting for population-based microfluidics and interfacial tensiometry. *Adv. Sci.* **7**, 2000359 (2020).
65. Raju, G., Kyriakopoulos, N. & Timonen, J. V. I. Diversity of non-equilibrium patterns and emergence of activity in confined electrohydrodynamically driven liquids. *Sci. Adv.* **7**, eabh1642 (2021).
66. Lane, W. R. Shatter of drops in streams of air. *Ind. Eng. Chem.* **43**, 1312–1317 (1951).
67. Reyssat, É., Chevy, F., Biance, A.-L., Petitjean, L. & Quéré, D. Shape and instability of free-falling liquid globules. *Europhys. Lett.* **80**, 34005 (2007).
68. Jain, M., Prakash, R. S., Tomar, G. & Ravikrishna, R. V. Secondary breakup of a drop at moderate Weber numbers. *Proc. R. Soc. A.* **471**, 20140930 (2015).
69. Zhao, H. et al. The largest diameter of falling drop in the up-gas flow. *Int. J. Multiph. Flow.* **159**, 104345 (2023).
70. Villermaux, E. Fragmentation. *Annu. Rev. Fluid Mech.* **39**, 419–446 (2007).
71. Cowley, M. D. & Rosensweig, R. E. The interfacial stability of a ferromagnetic fluid. *J. Fluid Mech.* **30**, 671–688 (1967).
72. Flament, C. et al. Measurements of ferrofluid surface tension in confined geometry. *Phys. Rev. E* **53**, 4801–4806 (1996).
73. Rigoni, C., Beaune, G., Harnist, B., Sohrabi, F. & Timonen, J. V. I. Ferrofluidic aqueous two-phase system with ultralow interfacial tension and micro-pattern formation. *Commun. Mater.* **3**, 26 (2022).
74. Taylor, G. I. Studies in electrohydrodynamics. I. The circulation produced in a drop by an electric field. *Proc. R. Soc. Lond. A* **291**, 159–166 (1966).
75. Melcher, J. R. & Taylor, G. I. Electrohydrodynamics: A review of the role of interfacial shear stresses. *Annu. Rev. Fluid Mech.* **1**, 111–146 (1969).
76. Salipante, P. F. & Vlahovska, P. M. Electrohydrodynamics of drops in strong uniform dc electric fields. *Phys. Fluids* **22**, 112110 (2010).
77. Vlahovska, P. M. Electrohydrodynamics of drops and vesicles. *Annu. Rev. Fluid Mech.* **51**, 305–330 (2019).
78. Reyes Garza, R., Kyriakopoulos, N., Cenev, Z. M., Rigoni, C. & Timonen, J. V. I. Magnetic Quincke rollers with tunable single-particle dynamics and collective states. *Sci. Adv.* **9**, eadh2522 (2023).
79. Verho, T. et al. Mechanically durable superhydrophobic surfaces. *Adv. Mater.* **23**, 673–678 (2011).
80. Tuteja, A. et al. Designing superoleophobic surfaces. *Science* **318**, 1618–1622 (2007).
81. Butt, H.-J. et al. Design principles for superamphiphobic surfaces. *Soft Matter* **9**, 418–428 (2013).
82. Bouillant, A. et al. Leidenfrost wheels. *Nat. Phys.* **14**, 1188–1192 (2018).
83. Wang, L. & McCarthy, T. J. Covalently attached liquids: Instant omniphobic surfaces with unprecedented repellency. *Angew. Chem. Int. Ed.* **55**, 244–248 (2016).

84. Li, Y., Quéré, D., Lv, C. & Zheng, Q. Monostable superrepellent materials. *Proc. Natl. Acad. Sci. USA* **114**, 3387–3392 (2017).
85. Vuckovac, M., Backholm, M., Timonen, J. V. I. & Ras, R. H. A. Viscosity-enhanced droplet motion in sealed superhydrophobic capillaries. *Sci. Adv.* **6**, eaba5197 (2020).
86. Schindelin, J. et al. Fiji: an open-source platform for biological-image analysis. *Nat. Methods* **9**, 676–682 (2012).
87. Schneider, C. A., Rasband, W. S. & Eliceiri, K. W. NIH Image to ImageJ: 25 years of image analysis. *Nat. Methods* **9**, 671–675 (2012).
88. Tinevez, J.-Y. et al. TrackMate: An open and extensible platform for single-particle tracking. *Methods* **115**, 80–90 (2017).
89. Ershov, D. et al. TrackMate 7: integrating state-of-the-art segmentation algorithms into tracking pipelines. *Nat. Methods* **19**, 829–832 (2022).

Acknowledgements

We thank Dr. Sakari Lepikko for providing the superhydrophobic substrates and Prof. Matilda Backholm and Ricardo Reyes Garza for valuable feedback and fruitful discussions. The project was funded by Academy of Finland Center of Excellence Program (2022-2029) in Life-Inspired Hybrid Materials LIBER (346112) and Foundation for Aalto University Science and Technology.

Author contributions

T.K. and J.V.I.T. designed the research and experiments. T.K. and I.P. performed the experiments and wrote the codes for data analysis. T.K. analysed the data with help from J.V.I.T. T.K. and N.K. performed the experiments for the complex phenomena in Q2D drops. J.V.I.T. conceived the idea and theory and performed preliminary experiments. T.K. and J.V.I.T. wrote the manuscript.

Competing interests

The authors declare no competing interests.

Additional information

Supplementary information The online version contains supplementary material available at https://doi.org/10.1038/s42005-024-01831-2.

Correspondence and requests for materials should be addressed to Jaakko V. I. Timonen.

Peer review information *Communications Physics* thanks Ciro Semprebon and the other, anonymous, reviewers for their contribution to the peer review of this work. A peer review file is available.